Article:
Pittiglio, G orcid.org/0000-0002-0714-5267, Orekhov, AL, da Veiga, T orcid.org/0000-0002-4286-4590 et al. (4 more authors) (2023) Closed Loop Static Control of Multi-Magnet Soft Continuum Robots. IEEE Robotics and Automation Letters, 8 (7). pp. 3980-3987. ISSN 2377-3766

https://doi.org/10.1109/lra.2023.3274431

Closed Loop Static Control of Multi-Magnet Soft Continuum Robots

Giovanni Pittiglio[1], *Member, IEEE,* Andrew L. Orekhov[2], Tomas da Veiga[3], Simone Calò[3], James H. Chandler[3], *Member, IEEE,* Nabil Simaan[4], *Fellow, IEEE,* and Pietro Valdastri[3], *Fellow, IEEE*

***Abstract*—This paper discusses a novel static control approach applied to magnetic soft continuum robots (MSCRs). Our aim is to demonstrate the control of a multi-magnet soft continuum robot (SCR) in 3D. The proposed controller, based on a simplified yet accurate model of the robot, has a high update rate and is capable of real-time shape control. For the actuation of the MSCR, we employ the dual external permanent magnet (dEPM) platform and we sense the shape via fiber Bragg grating (FBG). The employed actuation system and sensing technique makes the proposed approach directly applicable to the medical context. We demonstrate that the proposed controller, running at approximately 300 Hz, is capable of shape tracking with a mean error of 8.5% and maximum error of 35.2% . We experimentally show that the static controller is 25.9% more accurate than a standard PID controller in shape tracking and is able to reduce the maximum error by 59.2%.**

***Index Terms*—Medical Robots and Systems; Formal Methods in Robotics and Automation; Modeling, Control, and Learning for Soft Robots; Magnetic Actuation.**

I. Introduction

Soft continuum robots (SCRs) are hyperflexible mechanical structures [1] capable of shaping to convoluted paths. This makes them good candidates for medical applications involving delicate interaction with the anatomy [2], [3]. Magnetically actuated SCRs, or MSCRs, have been demonstrated in applications such as: neurosurgery [4–6], bronchoscopy [7], [8], cardiovascular interventions [9–11] and insertion of cochlear implants [12]. Magnetic actuation gives the possibility to apply forces and torques remotely [13], allowing MSCRs to have simpler structures compared to standard SCRs, supporting miniaturization and increased flexibility. Previous research [4], [5], [9], [12], [14] has shown how embedding a single internal permanent magnet (IPM) within a SCR allows for remote actuation. However, the use of a single IPM limits the maximum number of controllable degrees of freedom (DOFs) [15–17] the MSCR can realize.

Edelmann *et al.* [18] and Richter *et al.* [19] used Cosserat rod theory to model the behaviour of MSCRs, using camera feedback for sensing. In both papers, only simulation is used to demonstrated multi-magnet control in 3D. Although the actuation and control of 2 IPMs has also been experimentally demonstrated in [10], [20], [21], this was limited to a 2D plane.

In [8], we demonstrated that multi-IPM MSCRs have the potential to shape form to suit convoluted anatomical structures, improving navigation when compared to equivalent tip- and axially-magnetized MSCRs. In that study, we showed successful navigation in a phantom of the bronchi, which has a convoluted centerline. However, to improve the capabilities of MSCRs, closed-loop control is needed. This could enable full navigational autonomy and robust interaction with unpredictable anatomical deformation or motion, as shown for single-IPM robots [17].

This paper proposes a novel control approach which models the statics of MSCRs assuming *piece-wise constant curvature*, i.e. each segment of the robot can deform as an arc of a circle. This approach reduces the computational complexity of the model, compared to the Cosserat-rod approach employed in [18], [19]. In fact, the latter is formulated in a differential form, with respect to arc length, and requires iterative numerical solution of the static equilibrium. This is required to find the MSCR's Jacobian and can become computational intensive. Our model, in contrast, can be solved in closed form and runs at around 300 Hz, compared to 1 Hz [19] and 20 Hz [18] of previously proposed approaches. This is significant for medical applications to enhance safety via improved control bandwidth.

In the present work, we experimentally demonstrate the control of a multi-IPM MSCR in 3D. For closed-loop control, we use a Fiber Bragg Grating FBG sensor along the main axis of the robot which is directly applicable to clinical scenarios since it does not require visual access. We employ the dEPM actuation method, presented in [22], [23]. This is based on the collaborative actuation of two external permanent magnets (EPMs) which can generally apply a stronger magnetic field

Manuscript received: October 31, 2022; Revised: April 5, 2023; Accepted: April 28, 2023

This paper was recommended for publication by Editor Jessica Burgner-Kahrs upon evaluation of the Associate Editor and Reviewers' comments.

Research reported in this article was supported by the Engineering and Physical Sciences Research Council (EPSRC) under grants number EP/R045291/1 and EP/V009818/1, and by the European Research Council (ERC) under the European Union's Horizon 2020 research and innovation programme (grant agreement No 818045). Any opinions, findings and conclusions, or recommendations expressed in this article are those of the authors and do not necessarily reflect the views of the EPSRC or the ERC.

[1]G. Pittiglio is with the Department of Cardiovascular Surgery, Boston Children's Hospital, Harvard Medical School, Boston, MA 02115, USA and with the STORM Lab, Institute of Autonomous Systems and Sensing (IRASS), School of Electronic and Electrical Engineering, University of Leeds, Leeds, UK. Email: giovanni.pittiglio@childrens.harvard.edu

[2]A. L. Orekhov is with the Department of Mechanical Engineering, Vanderbilt University, Nashville, TN, USA, and the Robotics Institute at Carnegie Mellon University, Pittsburgh, PA, USA. Email: aorekhov@andrew.cmu.edu

[3]T. da Veiga, S. Calò, J. H. Chandler, P. Valdastri are with the STORM Lab, Institute of Autonomous Systems and Sensing (IRASS), School of Electronic and Electrical Engineering, University of Leeds, Leeds, UK. Email: {eltgdv, s.calo, j.h.chandler, p.valdastri}@leeds.ac.uk

[4]N. Simaan is with the department of Mechanical Engineering, Vanderbilt University, Nashville, TN 37235, USA. Email: nabil.simaan@vanderbilt.edu

Digital Object Identifier (DOI): see top of this page.

This article has been accepted for publication in IEEE Robotics and Automation Letters. This is the author's version which has not been fully edited and content may change prior to final publication. Citation information: DOI 10.1109/LRA.2023.3274431

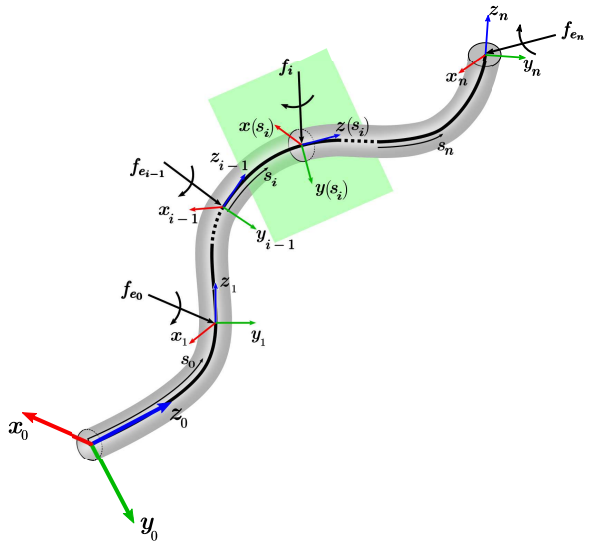

Fig. 1: Schematic representation of SCR.

compared to systems of coils [18], [19]. This offers a more direct application to the clinical context, as shown in [8].

We demonstrate that modelling the statics of the tentacle and incorporating the model in the control of the MSCR can improve the overall tracking, when compared to applying a standard PID controller on the configuration variables. We note that our model neglects dynamic inertial effects, since we envision the MSCR operating at slow speeds in this application, but believe a dynamics model could be incorporated in future work.

Our experiments in Section VI also analyze the advantages and limitations of using FBGs in this context. While they are useful for tracking small catheters without visual access, we had to limit the controlled DOFs to avoid axial twist, which the FBGs cannot track. We also noticed errors related to not tracking the twist, which are the outcome of applying a magnetic field opposed to the IPMs magnetic dipole direction.

The paper is organized as follows. In Sections II and and III, we present the constant-curvature kinematics used in the model of the MSCR. In Section IV, we present the statics model for the robot, including the effects of elasticity, gravity, and magnetic forces, and describe the model-based controller. Finally, in Sections V and VI we present the experimental results, and conclude with discussion in Section VII.

II. Direct Kinematics

In this section, we describe the direct kinematics of a *continuum robot* by assuming *piece-wise constant curvature*. In particular, referring to Fig. 1, the manipulator is divided into piece-wise constant curvature segments with the following properties: (i) homogeneity in the mechanical parameters, such as cross section, mass density and elasticity; (ii) constant internal wrench per length unit ($\mathbf{f}_i$) along each segment; (iii) only one external wrench ($\mathbf{f}_{e_i}$) applied at the end of each segment. Note that $\mathbf{f}_{e_i}, \mathbf{f}_i \in \mathbb{R}^6$ and each segment is described by the deflection in the 3 principal directions $\hat{\mathbf{n}}_i \in \mathbb{R}^3$ of the angle $\theta_i \in \mathbb{R}$.

The above conditions allow us to assume the i^{th} segment deflects with constant curvature having a local bending angle θ_i about a local axis of bending $\hat{\mathbf{n}}_i$. These entities define the local bending vector $\boldsymbol{\gamma}_i = \theta_i \hat{\mathbf{n}}_i$ along its length, parameterized by the length parameter $s_i \in [0, l_i]$, where $l_i \in \mathbb{R}$ is the length of the i^{th} segment.

Moreover, we assume no elongation of the robot, i.e. only angular deflection is modelled [24]. Specifically, we consider only torque actuation related to the interaction of each IPM with the externally applied magnetic field. We assume that field gradients, and related forces, are negligible.

The *direct kinematics* describes the pose of each infinitesimal section $(\mathbf{p}_i(s_i), \mathbf{R}_i(s_i)) \in \mathbb{R}^3 \times SO(3)$, with respect to the augmented curvature vector[1] $\boldsymbol{\gamma} = (\boldsymbol{\gamma}_1^{\mathrm{T}} \ \boldsymbol{\gamma}_2^{\mathrm{T}} \ \cdots \ \boldsymbol{\gamma}_n^{\mathrm{T}})^{\mathrm{T}} \in \mathbb{R}^{3n}$, in global reference frame $G_0 \equiv \{O_0, \mathbf{x}_0, \mathbf{y}_0, \mathbf{z}_0\}$. Specifically, $\mathbf{p}_i(s_i)$ relates to the position in global reference frame and $\mathbf{R}_i(s_i)$ is the rotation from local frame $F(s_i) = \{O(s_i), \mathbf{x}(s_i), \mathbf{y}(s_i), \mathbf{z}(s_i)\}$ to G_0.

First, we consider the evolution of the pose along the length of the manipulator, as

$$\begin{aligned} \frac{\partial \mathbf{p}_i(s_i)}{\partial s_i} &\overset{\text{def}}{=} \mathbf{p}_i'(s_i) = \mathbf{R}_i(s_i)\mathbf{e}_3 \\ \frac{\partial \mathbf{R}_i(s_i)}{\partial s_i} &\overset{\text{def}}{=} \mathbf{R}_i'(s_i) = \mathbf{R}_i(s_i)\,[\boldsymbol{\gamma}_i]^\wedge \end{aligned} \tag{1}$$

where $\mathbf{e}_i$ is the i^{th} element of the canonical basis of $\mathbb{R}^3$ (i.e. $\mathbf{e}_3$ is the tangent along the $\mathbf{z}$ axis) and $[\mathbf{v}]^\wedge$ denotes the cross product matrix form of a vector $\mathbf{v}$ i.e., $\mathbf{v}^\wedge \overset{\text{def}}{=} (\mathbf{v} \times \mathbf{e}_1, \ \mathbf{v} \times \mathbf{e}_2, \ \mathbf{v} \times \mathbf{e}_3)$ and its inverse is the *vee* $(\cdot^\vee)$ operator $(\mathbf{v}^\wedge)^\vee = \mathbf{v}$, for any vector $\mathbf{v} \in \mathbb{R}^3$.

When computing a local frame within a segment, we assume a piecewise constant curvature model, which leads to:

$$\mathbf{R}_i(s_i) = \mathbf{R}_{i-1}(l_{i-1})\exp\left(\left[\hat{\mathbf{n}}_i \frac{\theta_i s_i}{l_i}\right]^\wedge\right) \tag{2}$$

In the above equation, one could use Rodriguez's formula or an N^{th} order Taylor series expansion leading to:

$$\mathbf{R}_i(s_i) = \mathbf{R}_{i-1}(l_{i-1}) \sum_{k=0}^{N} \frac{1}{k!} \left(\frac{\theta_i s_i}{l_i}\right)^k \left([\hat{\mathbf{n}}_i]^\wedge\right)^k. \tag{3}$$

The latter is convenient in computing the differential kinematics described in Section III, where iterative integration by parts is employed; In the present work we use expansions up to order $N = 10$.

By substituting (3) into (1) and integrating, we can then obtain the position along the i^{th} segment:

$$\begin{aligned} \mathbf{p}_i(s_i) = \mathbf{p}_{i-1}(l_{i-1}) + \\ \mathbf{R}_{i-1}(l_{i-1}) \sum_{k=0}^{N} \frac{s^{k+1}}{(k+1)!} \left(\frac{\theta_i}{l_i}\right)^k \left([\hat{\mathbf{n}}_i]^\wedge\right)^k \mathbf{e}_3 \end{aligned} \tag{4}$$

Using (3) and (4), we can define the pose of each (infinitesimal) section of the continuum robot, which is equivalent to inferring its shape. This is useful since, in the general case, we aim to sense and control the shape of these manipulators.

[1]Note that, by assumption of piece-wise constant curvature, $\frac{\partial \boldsymbol{\gamma}_i}{\partial s_i} = 0$.

III. Differential Kinematics

As in the previous section, our aim is not only to describe the behavior of the end effector (EE), i.e the. tip of the MSCR, but also of the ends of each segment of the continuum robot. We first define the *augmented Jacobian* relating the temporal rate of the augmented curvature vector $\dot{\boldsymbol{\gamma}}$ to a vector of linear and angular velocities of the frames associated with points $\mathbf{p}_1, \ldots, \mathbf{p}_n$. This vector is defined as $\boldsymbol{\xi} \triangleq \left[\dot{\mathbf{p}}_1^{\mathrm{T}}, \boldsymbol{\omega}_1^{\mathrm{T}}, \ldots, \dot{\mathbf{p}}_n^{\mathrm{T}}, \boldsymbol{\omega}_n^{\mathrm{T}}\right]^{\mathrm{T}} \in \mathbb{R}^{6n\times 1}$ and called the augmented twist vector.

$$\boldsymbol{\xi} = \mathbf{J}(\mathbf{s})\dot{\boldsymbol{\gamma}}, \quad \mathbf{J}(\mathbf{s}) \in \mathbb{R}^{6n\times 3n} \tag{5}$$

where $\boldsymbol{\omega} = \left[\boldsymbol{\omega}_1^{\mathrm{T}}, \ldots, \boldsymbol{\omega}_n^{\mathrm{T}}\right]^{\mathrm{T}} \in \mathbb{R}^{3n\times 1}$ is the vector of angular velocities depicting the spatial angular velocities of the local frames at points $\mathbf{p}_1, \ldots, \mathbf{p}_n$. With these definitions, we define the block-partitioned form of $\mathbf{J}(\mathbf{s})$ as:

$$\mathbf{J}(\mathbf{s}) = \begin{bmatrix} \mathbf{J}_1(s_1) \\ \mathbf{J}_2(s_2) \\ \vdots \\ \mathbf{J}_n(s_n) \end{bmatrix}, \quad \mathbf{J}_i(s_i) \triangleq \begin{bmatrix} \mathbf{J}_{p_i}(s_i) \\ \cdots \\ \mathbf{J}_{o_i}(s_i) \end{bmatrix}, \; i \in [1, n] \tag{6}$$

where $\mathbf{s} = [s_1, s_2, \ldots, s_n]^{\mathrm{T}}$, and $\mathbf{J}_i$ defines the configuration space Jacobian for the i^{th} segment. The linear velocity Jacobian is given by:

$$\mathbf{J}_{p_i}(s_i) \triangleq \frac{\partial \mathbf{p}_i}{\partial \boldsymbol{\gamma}} \in \mathbb{R}^{3\times 3n} \tag{7}$$

To define the angular velocity Jacobian, we differentiate the rotation with respect to time to obtain:

$$\dot{\mathbf{R}}_i(s_i) = \boldsymbol{\omega}_i^{\wedge}(s_i)\mathbf{R}_i(s_i) \tag{8}$$

where $\boldsymbol{\omega}_i(s_i) \in \mathbb{R}^3$ is the spatial angular velocity of the i^{th} section. Solving for $\boldsymbol{\omega}_i(s_i)$:

$$\begin{aligned} \boldsymbol{\omega}_i(s_i) &= \left[\dot{\mathbf{R}}_i(s_i)\mathbf{R}_i^{\mathrm{T}}(s_i)\right]^{\vee} \\ &= \sum_{j=1}^{n} \left(\frac{\partial \mathbf{R}_i(s_i)}{\partial \gamma_j}\mathbf{R}_i^{\mathrm{T}}(s_i)\right)^{\vee} \dot{\gamma}_j \end{aligned} \tag{9}$$

where γ_j is the j^{th} element of $\boldsymbol{\gamma} \in \mathbb{R}^{3n}$. The i^{th} row of the angular velocity Jacobian is therefore given by:

$$\mathbf{J}_{o_i}(s_i) = \left[\left[\frac{\partial \mathbf{R}_i}{\partial \gamma_1}\mathbf{R}_i^{\mathrm{T}}\right]^{\vee} \quad \cdots \quad \left[\frac{\partial \mathbf{R}_i}{\partial \gamma_n}\mathbf{R}_i^{\mathrm{T}}\right]^{\vee}\right] \in \mathbb{R}^{3\times 3n} \tag{10}$$

The terms $\frac{\partial \mathbf{R}_i(s_i)}{\partial \gamma_j}$ can be analytically computed from (4).

IV. Static Control

Modeling dominating components of the MSCR's physical behavior can improve a controller's accuracy. In particular, considering behaviors such as elasticity and response to gravity, can reduce overshoots and lead to smoother motion, as shown in Section VI. Since in most medical applications, smooth and deliberate motion is preferred over high speed, here we only consider the static equilibrium of the MSCR and neglect higher-order dynamics, i.e. inertial, Coriolis and centrifugal factors.

In order to describe the static equilibrium of the MSCR in Fig. 1, we consider the *Lagrangian approach* and define the *Lagrangian*

$$L = T - U \tag{11}$$

where T is the *kinetic energy* and U is the *potential energy*. In the present work, we focus on the statics of the MSCR and only consider the static equilibrium ($T = 0$)

$$-\left(\frac{\partial L}{\partial \gamma}\right)^{\mathrm{T}} = \boldsymbol{\tau} \tag{12}$$

with $\boldsymbol{\tau}$ applied wrench.

The potential energy term is the sum of elastic and gravitational energy and reads as

$$\begin{aligned} U =& \sum_{i=1}^{n} \frac{1}{2} \int_0^{l_i} -\boldsymbol{\gamma}_i^{\mathrm{T}}\mathbf{k}_i\boldsymbol{\gamma}_i - 2m_i\mathbf{g}^{\mathrm{T}}\mathbf{p}_i(s_i)\mathrm{d}s_i \\ =& -\frac{1}{2}\boldsymbol{\gamma}^{\mathrm{T}}\mathrm{diag}\left(\mathbf{k}_1 l_1,\ \mathbf{k}_2 l_2,\ \ldots,\ \mathbf{k}_n l_n\right)\boldsymbol{\gamma} - \\ & \sum_{i=1}^{n} \int_0^{l_i} m_i\mathbf{g}^{\mathrm{T}}\mathbf{p}_i(s_i)\mathrm{d}s_i \\ =& -\frac{1}{2}\boldsymbol{\gamma}^{\mathrm{T}}\mathbf{K}\boldsymbol{\gamma} - \sum_{i=1}^{n} \int_0^{l_i} m_i\mathbf{g}^{\mathrm{T}}\mathbf{p}_i(s_i)\mathrm{d}s_i. \end{aligned} \tag{13}$$

Here, $\mathbf{g} \in \mathbb{R}^3$ is the gravitational acceleration in global frame, m_i is the i^{th} segment's mass density, and

$$\mathbf{k}_i = \mathrm{diag}\left(1,\ 1,\ \frac{1}{2(\nu+1)}\right)\frac{E_i A_i}{l_i} \tag{14}$$

with E_i *Young's modulus*, A_i second moment of area and ν is the *Poisson's ratio*. The first two diagonal elements of k_i are related to the bending stiffness, while the last one is related to the torsional stiffness, assuming that the body frame's $\mathbf{z}$-axis is defined to be tangent to the backbone curve.

By developing (12), we obtain

$$-\mathbf{K}\boldsymbol{\gamma} - \mathbf{G}(\boldsymbol{\gamma}) = \boldsymbol{\tau} \tag{15}$$

with

$$\mathbf{G}(\boldsymbol{\gamma}) = \mathbf{M}\begin{pmatrix} \int_0^{l_1} \mathbf{J}_{p_1}^{\mathrm{T}}(s_1)\mathrm{d}s_1 \\ \int_0^{l_2} \mathbf{J}_{p_2}^{\mathrm{T}}(s_2)\mathrm{d}s_2 \\ \vdots \\ \int_0^{l_n} \mathbf{J}_{p_n}^{\mathrm{T}}(s_n)\mathrm{d}s_n \end{pmatrix}\mathbf{g}, \tag{16}$$

$\mathbf{M} = \mathrm{diag}\left(m_1\mathbf{I}_3,\ m_2\mathbf{I}_3,\ \cdots,\ m_n\mathbf{I}_3\right)$, and $\mathbf{I}_3 \in \mathbb{R}^{3\times 3}$ being the identity matrix.

The last step in defining the statics of the MSCR is to define the wrench $\boldsymbol{\tau}$ acting on the system. This is achieved by applying the principle of virtual work on the sectioned continuum manipulator in Fig. 1. On the i^{th} segment, the overall wrench can be computed as

$$\begin{aligned} \boldsymbol{\tau}_i &= \sum_{j=i}^{n} \int_0^{l_j} \mathbf{J}_j^{\mathrm{T}}(s_j)\left(\mathbf{f}_j(s) + \mathbf{f}_{e_j}\delta(s_j - l_j)\right)\mathrm{d}s_j \\ &= \sum_{j=i}^{n} \left(\int_0^{l_j} \mathbf{J}_j^{\mathrm{T}}(s_j)\mathbf{f}_j(s)\mathrm{d}s_j\right) + \mathbf{J}_j^{\mathrm{T}}(l_j)\mathbf{f}_{e_j} \end{aligned} \tag{17}$$

where $\mathbf{f}_j(s)$ is a distributed external wrench on the j^{th} segment, $\mathbf{f}_{e_j}$ is a concentrated external wrench applied to the end of the j^{th} segment, and $\delta(s_j - l_j)$ is the Dirac delta function.

In the present work, we consider field-only actuation, thus only magnetic torque is generated on the magnetized segments. We assume that each segment owes a magnetization per unit length with magnetic dipole $\boldsymbol{\eta}_{i_0}$. This means each segment can be magnetized in one specific direction. Thus, the magnetization along the length of the i^{th} segment is $\boldsymbol{\eta}_i(s) = \mathbf{R}_i(s_i)\boldsymbol{\eta}_{i_0}$ and the wrench is

$$\begin{aligned}\boldsymbol{\tau}_i &= \sum_{j=i}^{n}\left(\int_0^{l_j} \mathbf{J}_{o_j}^{\mathrm{T}}(s_j)\boldsymbol{\eta}^{\wedge}(s)\mathbf{B}\mathrm{d}s_j\right) + \mathbf{J}_j^{\mathrm{T}}(l_j)\mathbf{f}_{e_j},\\ &= \sum_{j=i}^{n}\left(\int_0^{l_j} \mathbf{J}_{o_j}^{\mathrm{T}}(s_j)\boldsymbol{\eta}^{\wedge}(s)\mathrm{d}s_j\right)\mathbf{B} + \mathbf{J}_j^{\mathrm{T}}(l_j)\mathbf{f}_{e_j}, \quad (18)\end{aligned}$$

with $\mathbf{B} \in \mathbb{R}^3$ defining the external actuating field. The above equation can be put in matrix form as:

$$\boldsymbol{\tau} = \mathbf{H}(\boldsymbol{\gamma})\mathbf{B} + \mathbf{J}^{\mathrm{T}}(\boldsymbol{\gamma})\mathbf{f}_e \quad (19)$$

Since $\mathbf{J}_{o_j}(s_j)$ and $\boldsymbol{\eta}^{\wedge}(s)$ are polynomials in s of order N (where N is the order of approximation of the exponential map), the integral in (17) is found by iteratively integrating by parts. By combining (15) and (18), we obtain the static equilibrium equation

$$-\mathbf{K}\boldsymbol{\gamma} - \mathbf{G}(\boldsymbol{\gamma}) = \mathbf{H}(\boldsymbol{\gamma})\mathbf{B} + \mathbf{J}^{\mathrm{T}}(\boldsymbol{\gamma})\mathbf{f}_e. \quad (20)$$

where $\mathbf{f}_e = [\mathbf{f}_{e_1}^{\mathrm{T}}, \ \cdots \ \mathbf{f}_{e_n}^{\mathrm{T}}]^{\mathrm{T}}$. We consider the error $\tilde{\boldsymbol{\gamma}} = \boldsymbol{\gamma}_d - \boldsymbol{\gamma}$ and apply the control strategy

$$\mathbf{B} = \mathbf{H}^{+}(\boldsymbol{\gamma})\left(-\mathbf{K}\boldsymbol{\gamma} - \mathbf{G}(\boldsymbol{\gamma}) - \mathbf{J}^{\mathrm{T}}(\boldsymbol{\gamma})\mathbf{f}_e + \mathbf{K}_p\tilde{\boldsymbol{\gamma}} + \mathbf{K}_d\dot{\tilde{\boldsymbol{\gamma}}}\right) \quad (21)$$

with $\cdot^{+}$ denoting the matrix pseudo-inverse. By substitution this expression into (20), we obtain

$$\mathbf{K}_p\tilde{\boldsymbol{\gamma}} + \mathbf{K}_d\dot{\tilde{\boldsymbol{\gamma}}} = 0 \quad (22)$$

which is asymptotically stable with the choice of the proportional ($\mathbf{K}_p$) and derivative ($\mathbf{K}_d$) parameters of the controller positive definite. Notice that the controller has an exact form in the case where the curvature is fully sensed.

V. Experimental Setup

We validate our control strategy by actuating a 4-segment MSCR with the dEPM platform [8], [22]. The setup is presented in Fig. 2a. The MSCR is a combination of 2 magnetically-doped segments alternated with magnetically-inert ones, both 4 mm in diameter. The former were fabricated by casting silicone prepolymer (Dragon Skin 30; Smooth-On, Inc.) mixed with magnetic microparticles (NdFeB, MQFP-B+; Magnequench GmnH, Germany) in a 3D-printed mold (ToughPLA; Ultimaker S5). After demolding, they were magnetised in an impulse magnetizer (IM-10-30; ASCScientific), then alingned in an overmold at a distance equal to their length (10 mm). The overmold was injected with magnetically-inert silicone (Ecoflex 00-30; Smooth-On, Inc.) for bonding.

While, most of the applications of the proposed MSCRs would be in a confined space and not always with their main axis along gravity, here we consider the case when the MSCR is free of any motion. This can more generally help evaluating the performance of the proposed control method and avoid that gravity would dominate the dynamics, as in the case the MSCR is orientated horizontally. In fact, we preferred analyzing the behavior of a soft catheter, which is of better use for medical applications, over a stiffer one.

As illustrated in Fig. 2b, the magnetic segments of the MSCR are magnetised orthogonally. This way, as discussed in [22], we obtain maximum independence between the segments and we can actuate them independently by applying the appropriate magnetic field. Specifically, a torque along the $\mathbf{y}$-axis on magnet 1 ($\mathbf{m}_1$) can be generated by applying a magnetic field along $\mathbf{x}$; magnet 2 ($\mathbf{m}_2$) can be actuated around the $\mathbf{y}$-axis by applying a field along $\mathbf{z}$. Notice that a field along $\mathbf{y}$ would generate a torque on magnet 1 around $\mathbf{x}$ and on magnet 2 around $\mathbf{z}$.

For shape sensing, we use an off-the-shelf FBG fiber (3 cores, 18 sensors spaced 1 cm apart, FBGS International, Jena, Germany) and employ only the last 4 sensors. Since this sensing technique is not able to sense torsion (torque around the $\mathbf{z}$-axis), we constrain the desired trajectories so that torsion would not be generated or controlled. The fiber was placed in a cavity made in the magnetic segments and non-magnetic silicone, by using a 1 mm diameter NiTi wire along the main axis of the MSCR central to its diameter. After removal of the NiTi wire, the fiber was inserted in the longitudinal hole.

Before running the control experiments, we calibrated the system so that the MSCR is localized within the magnetic workspace. We used an optical tracker (OptiTrack, Natural-Point, Inc., USA) to localize the base of the MSCR (frame $\mathcal{W}$) with respect to the robots' EPMs (frame $\mathcal{E}_i,\ i = 1, 2$), i.e. the homogeneous transformation ${}^{\mathcal{E}_i}\mathbf{T}_{\mathcal{W}} \in SE(3),\ i = 1, 2$. From the robots direct kinematics, we obtain ${}^{\mathcal{B}_i}\mathbf{T}_{\mathcal{E}_i} \in SE(3)$ and eventually find the pose of the base of the MSCR with respect to each robots base as ${}^{\mathcal{B}_i}\mathbf{T}_{\mathcal{E}_i}\ {}^{\mathcal{E}_i}\mathbf{T}_{\mathcal{W}} \in$ SE(3).

For these experiments, we actuate the magnetic field according to

$$\mathbf{B} = \sum_{i=1}^{2} \frac{\mu_0|\boldsymbol{\mu}_i|}{4\pi|\mathbf{r}_i|^3}\left(3\hat{\mathbf{r}}_i\hat{\mathbf{r}}_i^{\mathrm{T}} - \boldsymbol{I}_3\right)\hat{\boldsymbol{\mu}}_i \ \in \mathbb{R}^3, \quad (23)$$

where $\mathbf{r}_i \in \mathbb{R}^3$ is the position of the i^{th} EPM and $\boldsymbol{\mu}_i \in \mathbb{R}^3$ is its magnetic dipole with respect to the center of the workspace; μ_0 is the air magnetic permeability, and $|\cdot|$ is the Euclidean norm, $\hat{\cdot} = \frac{\cdot}{|\cdot|}$.

Since the EPMs are far enough from the MSCR, we assume their field can be accurately described by the dipole model [25]. A magnetic field with minimal gradients can be generated, according to [22], by imposing $\mathbf{r}_1 = \mathbf{r}_2 = \mathbf{r}$ and $\boldsymbol{\mu}_1 = \boldsymbol{\mu}_2 = \boldsymbol{\mu}$. Notice that for permanent magnets $|\boldsymbol{\mu}_i| = \text{const}$. Without loss of generality, we can impose $\hat{\mathbf{r}}_i = \mathbf{e}_2,\ i = 1, 2$; in fact, being the matrix $\left(3\hat{\mathbf{r}}\hat{\mathbf{r}}^{\mathrm{T}} - \mathbf{I}_3\right) = \left(3\mathbf{e}_2\mathbf{e}_2^{\mathrm{T}} - \mathbf{I}_3\right)$ full rank, we can actuate any desired field. This is applicable to any direction of $\mathbf{r}_i$ and we chose $\mathbf{e}_2$ to maximize the reach of the robots and to avoid collision of the EPMs.

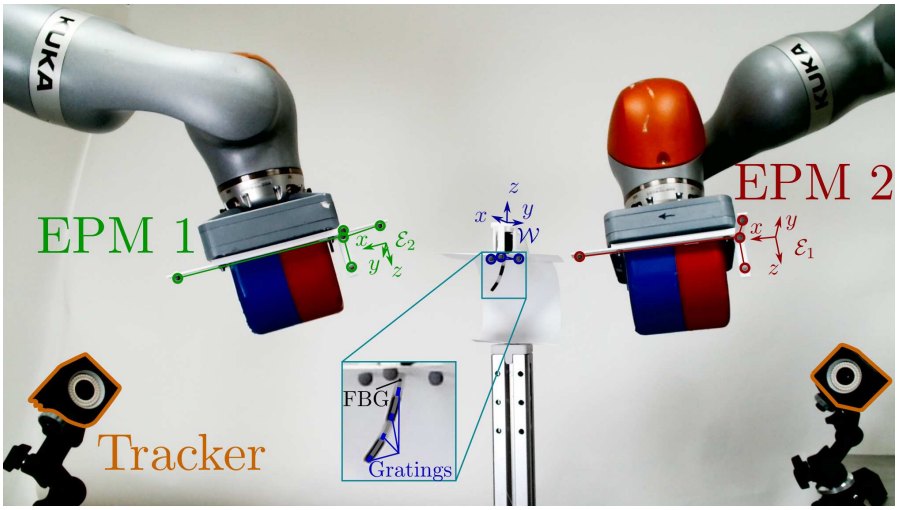

(a) Experimental setup for validation of the closed-loop control strategy.

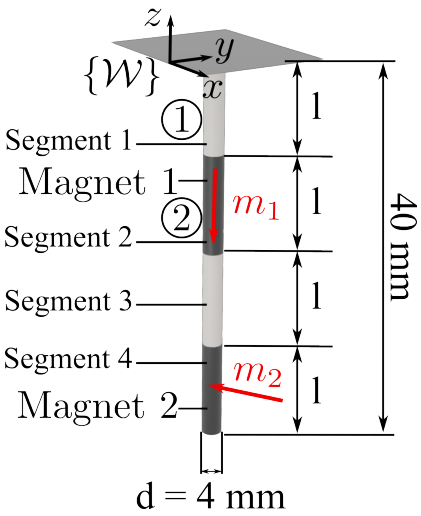

(b) Schematic representation of the MSCR used in the experimental analysis. ① magnetic segment, ② non-magnetic segment; $l = 10$ mm.

Fig. 2: Experimental setup and MSCR employed for the evaluation of the control strategies.

The expression in (23) simplifies to

$$\mathbf{B} = \frac{\mu_0 |\boldsymbol{\mu}|}{2\pi |\mathbf{r}|^3} \left(3\mathbf{e}_2\mathbf{e}_2^{\mathrm{T}} - \mathbf{I}_3\right) \hat{\boldsymbol{\mu}}, \tag{24}$$

For a required field $\mathbf{B}$, computed by the controller described in previous section, we find the pose of each EPM as discussed in [8]:

$$\begin{aligned} |\mathbf{r}| &= \left(\frac{2\pi|\mathbf{B}|}{\mu_0|\boldsymbol{\mu}|}\right)^{\frac{1}{3}} \\ \hat{\boldsymbol{\mu}} &= \frac{\left(3\mathbf{e}_2\mathbf{e}_2^{\mathrm{T}} - \mathbf{I}_3\right)^{-1}}{|3\mathbf{e}_2\mathbf{e}_2^{\mathrm{T}} - \mathbf{I}_3|}\hat{\mathbf{B}} \end{aligned} \tag{25}$$

From the calibration obtained from the optical tracker, we transform $\mathbf{r}$ and $\hat{\boldsymbol{\mu}}$ into an EE pose for each robot and command them via their inverse kinematics.

VI. Experimental Results

The MSCR was virtually divided in four constant-curvature segments, one for each section (see Fig. 2b). The configuration space of the robot can be described as

$$\begin{aligned} \boldsymbol{\gamma} &= \left(\boldsymbol{\gamma}_1^{\mathrm{T}}\ \boldsymbol{\gamma}_2^{\mathrm{T}}\ \boldsymbol{\gamma}_3^{\mathrm{T}}\ \boldsymbol{\gamma}_4^{T}\right)^{\mathrm{T}} \\ \boldsymbol{\gamma}_i &= \gamma_{i_1}\boldsymbol{e}_1 + \gamma_{i_2}\boldsymbol{e}_2 + \gamma_{i_3}\boldsymbol{e}_3 \end{aligned} \tag{26}$$

We perform four repetitions in controlling the segments deflection to obtain a figure-eight pattern motion for the MSCR's EE. This motion was chosen to evaluate the controller's ability to control the MSCR's DOFs independently along the length, while avoiding twisting along the axial direction; this DOF is controllable but not observable with the sensing technique employed (FBG shape sensing). In this example, the FBG enables fine measurement of the shape, but limits the DOFs which can be actuated. However, we show that general tip motion can be obtained by controlling each magnet independently.

In fact, the imposed figure-eight tip motion is obtained when the top and bottom magnets move at different frequencies and shows a general case for this example. While a circular shape requires the IPMs to move in sync and in a square motion only one at the time, the figure-eight trajectory requires this more complex behavior.

The desired figure-eight deflection was

$$\begin{aligned} \gamma_{2_1} &= \gamma_M \sin(2\pi t/T) \\ \gamma_{4_2} &= \gamma_M \sin(4\pi t/T) \end{aligned} \tag{27}$$

with $\gamma_M = 7^o$ and $T = 120$ s, and t time. The controller frequency was 300 Hz.

We compared the proposed static controller with a PID controller and report the tracking performance in Fig. 3. Specifically, we compare the desired and measured angular deflection of the actuated segments of the MSCR. A video of the experiments can be found in the Supplementary Material.

The PID control considers no elastic behavior, gravity or external forces and the applied field is computed as

$$\mathbf{B} = \mathbf{H}^{+}(\boldsymbol{\gamma}) \left(\mathbf{K}_p\tilde{\boldsymbol{\gamma}} + \mathbf{K}_d\dot{\tilde{\boldsymbol{\gamma}}}\right) \tag{28}$$

In Fig. 3, we notice that the static controller achieves a generally smoother tracking of the desired shape; the PID controller, with same proportional and derivative gains, shows a more noisy behavior and is more reactive in case of high deflections. This is particularly notable in the tracking of γ_{4_2}.

We believe that the behavioral difference between the two controllers is caused by the fact that the PID controller does not account for gravity and elasticity. In the resting configuration, these factors are negligible, however they become more prominent on the peaks. In these cases, the PID controller shows less stability and more ripple compared to the static controller, which can predict the increase in potential energy using the proposed model.

This article has been accepted for publication in IEEE Robotics and Automation Letters. This is the author's version which has not been fully edited and content may change prior to final publication. Citation information: DOI 10.1109/LRA.2023.3274431

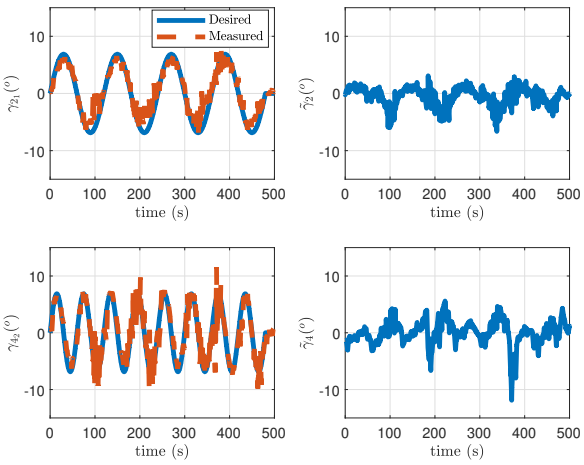

(a) PID controller.

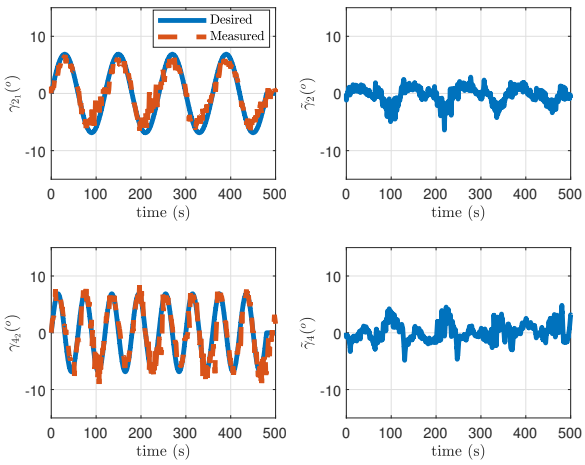

(b) Static controller.

Fig. 3: Comparison of deflection tracking between PID and static controllers. Reported the desired deflection around the $\mathbf{x}$-axis for the top segment and the $\mathbf{y}$-axis for the bottom one. On the rightmost column of (a) and (b), we show the error between desired and measured deflection for the respective angles.

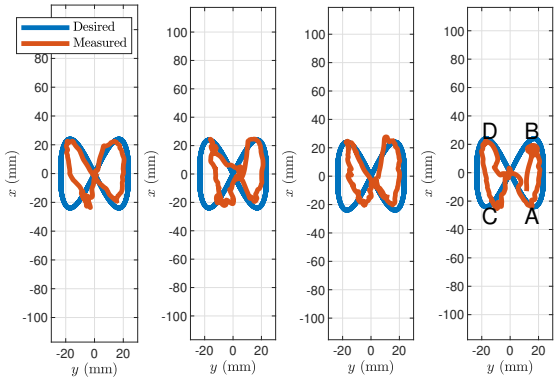

(a) Planar motion of the EE showing the desired tip position against the tip position measured using the FBG.

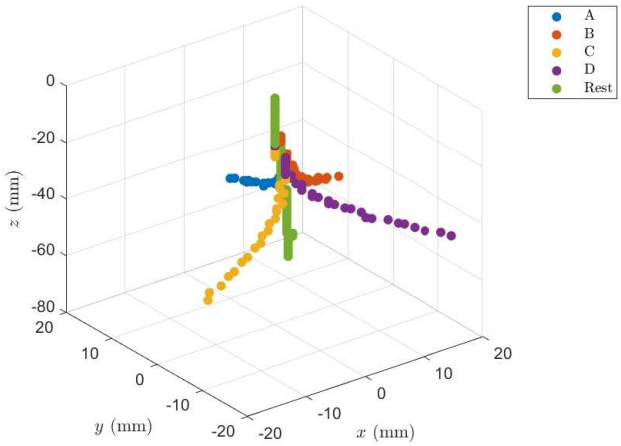

(b) Shape measured by the FBG in case of maximum deflection for the last repetition; comparison with resting confiration ("Rest").

Fig. 4: Desired and measured planar motion of the MSCR EE as measured by the FBG under PID control.

We computed the absolute error in tracking the curvature (see Fig. 3) and EE position (see Figs. 4a and 5a) for both static and PID controllers - over four repetitions. We found the static controller to reduce the maximum error by 59.2% and the mean error by 25.9%.

TABLE I: Summary of Tracking Errors

	Static Control	PID Control
Mean (Max) Tip Error (mm)	3.8 (36.9)	4.4 (42.2)
Mean (Max) Deflection Error (%)	8.5 (35.2)	10.7 (86.4)

In Fig. 4 and 5 we report the respective planar tracking (on the $\mathbf{x}-\mathbf{y}$ plane) for the EE tip for the PID and static controller, along with the shape measured by the FBG. The sensed shape was captured during the last repetition in which the EE passed through the four points (A-D) where the MSCR was at its maximum deflection.

A behavior which is important to analyze is the asymmetry between the figure-eight's lobes. We notice that, generally, the left lobe is harder to track and the measured position of the EE would generally have a worse tracking than the right side. This is due to the marginally stable equilibrium resultant from the actuation of the second magnet by an anti-parallel magnetic field. More specifically, when $\hat{\mathbf{B}} = -\hat{\mathbf{m}}_\mathbf{1}$, the theoretical resultant is a torque around $\mathbf{x}$ (τ_{2_1}); however, in reality this may create instabilities due to the fact that a slight misalignment can cause unexpected twist.

This is an important reason for having an effective and reactive high-frequency controller, since open-loop control or

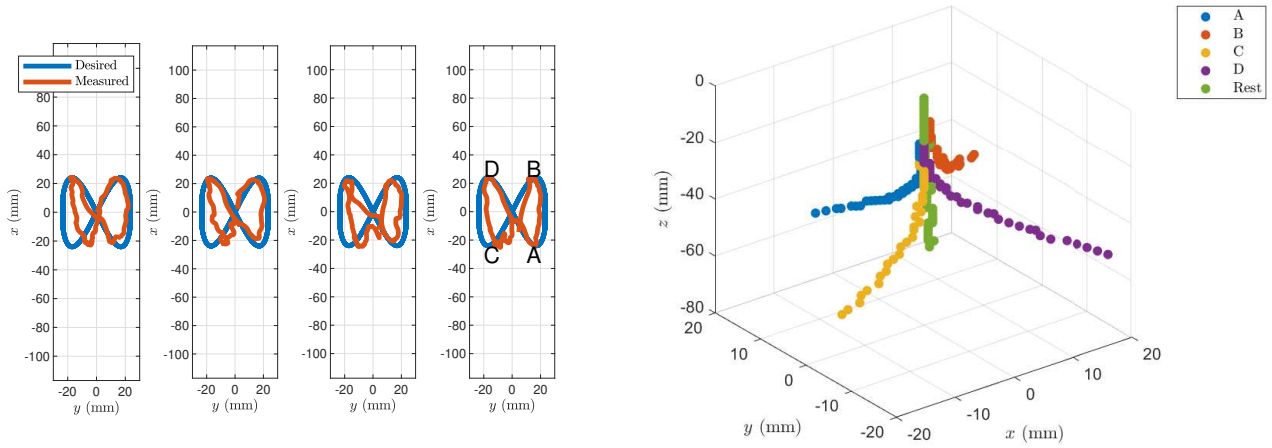

(a) Planar motion of the EE. Reported the desired tip position against the measured one, output of the FBG.

(b) Shape measured by the FBG in case of maximum deflection for the last repetition; comparison with resting confiration ("Rest").

Fig. 5: Desired and measured planar motion of the MSCR EE as measured by the FBG under static control.

failing to observe/sense the instability may result in loss of the marginally stable DOFs. This is fundamental in MSCRs with non-axial magnetization profiles [8], [19].

The difference in the tracking performance in each repetition is caused by the actuation strategy, which requires transitions of the EPMs between desired poses, given a desired magnetic field. This transition is not consistent and depends on the current configuration of the serial robot manipulating each EPM. In the present paper, we considered a point-to-point strategy for the motion of the EPMs; however, more appropriate planning of the EPM motion could improve the precision of the actuation platform.

VII. Conclusion

The presented paper discussed a novel controller for multi-magnet MSCRs with shape feedback from FBG sensors. This new class of continuum robots has gained interest given their potential for miniaturization without direct loss of DOFs. However, despite these advantages, their control is not trivial due to the presence of unstable behaviors caused by the non-ideal interaction of the robot with the actuating magnetic field.

In the present paper, we discussed a novel approach for the control of this class of robots, based on the modelling of their statics under a piece-wise constant curvature assumption. Compared to the state-of-the-art, the proposed method can run in real-time (300 Hz). This factor, related to the minimal complexity of the model, is of primary importance in presence of instabilities; in fact, a reactive sensing and control strategy can minimize unexpected behaviors caused by non-ideal dynamics.

The applied method is based on FBG sensing, which gives direct measurement of the MSCR's shape without the need for visual access, and thus can be more readily translated to clinical applications. We report a demonstration of tracking performance using the proposed control method by applying the dEPMs actuation technique [8], [22], based on the collaborative control of two EPMs. We show how the desired field, resulting from the wrench commanded by the controller, can be generated with this control strategy.

Experimental evaluation of the controller was performed using a figure-eight trajectory following task, with comparisons made to a standard PID control approach across four repetitions. Given the inclusion of gravity and elasticity in the model, the proposed controller presented a 20.8% reduction of the mean error, compared to the PID control method. Differences between repetitions were evident due to the irregular motion of the EPMs and its dependence upon current state of the serial robots. To improve the precision of the proposed control method, in future work we will improve the actuation strategy by adding a level of planning to the robots motion and introducing dynamic modelling. We believe that this will reduce ripple and provide improved precision.

Instabilities were noticed when the applied magnetic field causes twist on the top IPM. In this case, since the FBG sensors cannot sense these twist deformations, the controller is not informed of the actual state of the MSCR and therefore has higher error in controlling the desired tip position. Investigating sensing techniques which can track twist [26] would help eliminate this problem and enable full control of both bending angle and axial rotation.

We evaluated the behavior of the MSCR while its main axis is along gravity and in unconstrained environment, to simulate the case when it is free of moving in any direction and gravity is not dominating. Together with the imposed figure-eight tracking of the tip, this underlines a general case when the IPMs' motion is free of constraints and diverse over time. Future studies will consider navigation in a closed anatomy and the case when the MSCRs can move horizontally. We envision that the former may stabilize the dynamics, while the latter would require analyzing solutions such as a constant EPM-IPM attraction or levitation [16], [17].

REFERENCES

[1] S. Kolachalama and S. Lakshmanan, "Continuum Robots for Manipulation Applications: A Survey," *Journal of Robotics*, vol. 2020, p. 4187048, 2020.

[2] T. Da Veiga, J. H. Chandler, G. Pittiglio, P. Lloyd, M. Holdar, O. Onaizah, A. Alazmani, and P. Valdastri, "Material characterization for magnetic soft robots," in *2021 IEEE 4th International Conference on Soft Robotics (RoboSoft)*, 2021, pp. 335–342.

[3] P. Dupont, N. Simaan, H. Choset, and C. Rucker, "Continuum robots for medical interventions," *Proceedings of the IEEE*, pp. 1–24, 2022.

[4] A. Hong, A. J. Petruska, A. Zemmar, and B. J. Nelson, "Magnetic Control of a Flexible Needle in Neurosurgery," *IEEE Transactions on Biomedical Engineering*, vol. 68, no. 2, pp. 616–627, 2021.

[5] Y. Kim, G. A. Parada, S. Liu, and X. Zhao, "Ferromagnetic soft continuum robots," *Science Robotics*, vol. 4, no. 33, p. eaax7329, 2019.

[6] A. J. Petruska, F. Ruetz, A. Hong, L. Regli, O. Surucu, A. Zemmar, and B. J. Nelson, "Magnetic needle guidance for neurosurgery: Initial design and proof of concept," in *2016 IEEE International Conference on Robotics and Automation (ICRA)*. Institute of Electrical and Electronics Engineers Inc., 2016, pp. 4392–4397.

[7] J. Edelmann, A. J. Petruska, and B. J. Nelson, "Estimation-Based Control of a Magnetic Endoscope without Device Localization," *Journal of Medical Robotics Research*, vol. 03, no. 01, p. 1850002, 2018.

[8] G. Pittiglio, P. Lloyd, T. da Veiga, O. Onaizah, C. Pompili, J. H. Chandler, and P. Valdastri, "Patient-specific magnetic catheters for atraumatic autonomous endoscopy," *Soft Robotics*, 2022.

[9] Z. Yang, L. Yang, M. Zhang, Q. Wang, S. C. H. Yu, and L. Zhang, "Magnetic Control of a Steerable Guidewire Under Ultrasound Guidance Using Mobile Electromagnets," *IEEE Robotics and Automation Letters*, vol. 6, no. 2, pp. 1280–1287, 2021.

[10] S. Jeon, A. K. Hoshiar, K. Kim, S. Lee, E. Kim, S. Lee, J.-y. Kim, B. J. Nelson, H.-J. Cha, B.-J. Yi, and H. Choi, "A Magnetically Controlled Soft Microrobot Steering a Guidewire in a Three-Dimensional Phantom Vascular Network," *Soft Robotics*, vol. 6, no. 1, pp. 54–68, 2018.

[11] A. Ali, D. H. Plettenburg, and P. Breedveld, "Steerable Catheters in Cardiology: Classifying Steerability and Assessing Future Challenges," *IEEE Transactions on Biomedical Engineering*, vol. 63, no. 4, pp. 679–693, 2016.

[12] T. L. Bruns, K. E. Riojas, D. S. Ropella, M. S. Cavilla, A. J. Petruska, M. H. Freeman, R. F. Labadie, J. J. Abbott, and R. J. Webster, "Magnetically Steered Robotic Insertion of Cochlear-Implant Electrode Arrays: System Integration and First-In-Cadaver Results," *IEEE Robotics and Automation Letters*, vol. 5, no. 2, pp. 2240–2247, 2020.

[13] Q. Boehler, S. Gervasoni, S. L. Charreyron, C. Chautems, and B. J. Nelson, "On the workspace of electromagnetic navigation systems," *IEEE Transactions on Robotics*, pp. 1–17, 2022.

[14] C. Chautems, A. Tonazzini, Q. Boehler, S. H. Jeong, D. Floreano, and B. J. Nelson, "Magnetic Continuum Device with Variable Stiffness for Minimally Invasive Surgery," *Advanced Intelligent Systems*, p. 1900086, 2019.

[15] J. Wang, J. Xue, S. Yuan, J. Tan, S. Song, and M. Q.-H. Meng, "Kinematic modeling of magnetically-actuated robotic catheter in nonlinearly-coupled multi-field," *IEEE Robotics and Automation Letters*, pp. 1–1, 2021.

[16] G. Pittiglio, L. Barducci, J. W. Martin, J. C. Norton, C. A. Avizzano, K. L. Obstein, and P. Valdastri, "Magnetic Levitation for Soft-Tethered Capsule Colonoscopy Actuated With a Single Permanent Magnet: A Dynamic Control Approach," *IEEE Robotics and Automation Letters*, vol. 4, no. 2, pp. 1224–1231, 2019.

[17] L. Barducci, G. Pittiglio, J. C. Norton, K. L. Obstein, and P. Valdastri, "Adaptive Dynamic Control for Magnetically Actuated Medical Robots," *IEEE Robotics and Automation Letters*, vol. 4, no. 4, pp. 3633–3640, 2019.

[18] J. Edelmann, A. J. Petruska, and B. J. Nelson, "Magnetic control of continuum devices," *International Journal of Robotics Research*, vol. 36, no. 1, pp. 68–85, 2017.

[19] M. Richter, V. K. Venkiteswaran, and S. Misra, "Multi-Point Orientation Control of Discretely-Magnetized Continuum Manipulators," *IEEE Robotics and Automation Letters*, vol. 6, no. 2, pp. 3607–3614, 2021.

[20] M. Yousefi and H. Nejat Pishkenari, "Independent position control of two identical magnetic microrobots in a plane using rotating permanent magnets," *Journal of Micro-Bio Robotics*, vol. 17, no. 1, pp. 59–67, 2021.

[21] D. Lin, N. Jiao, Z. Wang, and L. Liu, "A Magnetic Continuum Robot With Multi-Mode Control Using Opposite-Magnetized Magnets," *IEEE Robotics and Automation Letters*, vol. 6, no. 2, pp. 2485–2492, 2021.

[22] G. Pittiglio, J. H. Chandler, M. Richter, V. K. Venkiteswaran, S. Misra, and P. Valdastri, "Dual-Arm Control for Enhanced Magnetic Manipulation," in *2020 IEEE/RSJ International Conference on Intelligent Robots and Systems (IROS)*, 2020, pp. 7211–7218.

[23] G. Pittiglio, M. Brockdorff, T. da Veiga, J. Davy, J. H. Chandler, and P. Valdastri, "Collaborative magnetic manipulation via two robotically actuated permanent magnets," *IEEE Transactions on Robotics*, vol. 39, no. 2, pp. 1407–1418, 2023.

[24] S. Grazioso, G. Di Gironimo, and B. Siciliano, "A Geometrically Exact Model for Soft Continuum Robots: The Finite Element Deformation Space Formulation," *Soft Robotics*, vol. 6, no. 6, pp. 790–811, 2019.

[25] A. J. Petruska and J. J. Abbott, "Optimal Permanent-Magnet Geometries for Dipole Field Approximation," *IEEE Transactions on Magnetics*, vol. 49, no. 2, pp. 811–819, 2013.

[26] T. da Veiga, G. Pittiglio, M. Brockdorff, J. H. Chandler, and P. Valdastri, "Six-degree-of-freedom localization under multiple permanent magnets actuation," *IEEE Robotics and Automation Letters*, vol. 8, no. 6, pp. 3422–3429, 2023.